The Attitude and Determination Control System (ADCS) for the Orbital Calibration 2 Mission (OrCa2)

AE 8900 MS Special Problems Report
Space Systems Design Laboratory (SSDL)
Guggenheim School of Aerospace Engineering
Georgia Institute of Technology
Atlanta, GA

Author:
Luke DiStasio

Advisor:
Prof. Brian C. Gunter

June 30, 2022

THE ATTITUDE AND DETERMINATION CONTROL SYSTEM (ADCS) FOR THE ORBITAL CALIBRATION 2 MISSION (ORCA2)

Luke DiStasio*, Brian Gunter†

The Orbital Calibration 2 (OrCa2) mission is a collaboration between the Georgia Institute of Technology and the Georgia Tech Research Institute aimed at improving space domain awareness. The 12U OrCa2 CubeSat contains an attitude determination and control system (ADCS) which processes gyro, magnetometer, and sun sensor measurements to estimate spacecraft attitude on orbit. Attitude control is achieved using three custom air coil magnetorquers designed and built by the ADCS team. The two control modes used by the OrCa2 ADCS are a detumble mode to reduce angular rates upon deployment and a three-axis sun and beacon pointing mode, which uses a quaternion PD controller to point the spacecraft solar panels towards the sun and the downlink beacon antenna above the horizon. Attitude is estimated using a multiplicative extended Kalman filter (EKF). Air bearing testing of the ADCS system verified both the ability of the EKF to estimate attitude and the ability of the controllers to command the correct torques. It is estimated that full detumble from an initial deployment angular rate of 10 deg/s would take approximately two orbits.

MISSION OVERVIEW

The Georgia Institute of Technology (Georgia Tech), in collaboration with the Georgia Tech Research Institute (GTRI), has developed the Orbital Calibration 2 (OrCa2) mission in an effort to improve space domain awareness. OrCa2's external panels have precise and well-characterized reflective properties that will permit various calibration activities from ground-based optical sensors, with the goal of improving the tracking and detection of resident space objects (RSOs). OrCa2 is a 12U CubeSat designed, fabricated, assembled, and tested almost entirely in-house using GT/GTRI facilities. It will be regularly observed using Georgia Tech's Space Object Research Telescope (GT-SORT) and additional all-sky cameras, with additional tracking support from the 18th SPCS and the International Laser Ranging Service (ILRS). A number of experiments can be conducted with these measurements, such as pose estimation, validation of RSO trajectory propagations with complementary ground-based laser ranging data, multi-spectral analysis, low-light detection algorithms, and validation of atmospheric scattering models.

Attitude determination will be achieved using an Epson M-G364 inertial measurement unit (IMU), a Solar MEMS nanoSSOC-D60 two-axis digital sun sensor, and a Honeywell HMC1053 three-axis magnetometer. Attitude control will be achieved using three orthogonal custom-built magnetorquers. These actuators will enable both a detumble mode and a sun pointing/beacon mode for solar battery charging and data downlinks. Additionally, the OrCa2 spacecraft hosts

* Master's Student, Georgia Institute of Technology Space Systems Design Lab.
† Faculty Advisor, Georgia Institute of Technology Space Systems Design Lab.

experimental radiation dosimeters, an experimental software defined radio (SDR) receiver, and an experimental power system. Communications for OrCa2 will be conducted through an Eyestar half-duplex unit provided by NearSpace Launch, Inc. This unit will enable low-bandwidth communications through the Iridium satellite constellation and will also provide GPS positioning information. OrCa2 will be deployed into a geosynchronous transfer orbit (GTO). The Eyestar unit is the only transmitter on the satellite, and maintaining active communications is not a mission requirement.

ADCS OVERVIEW AND CONFIGURATION

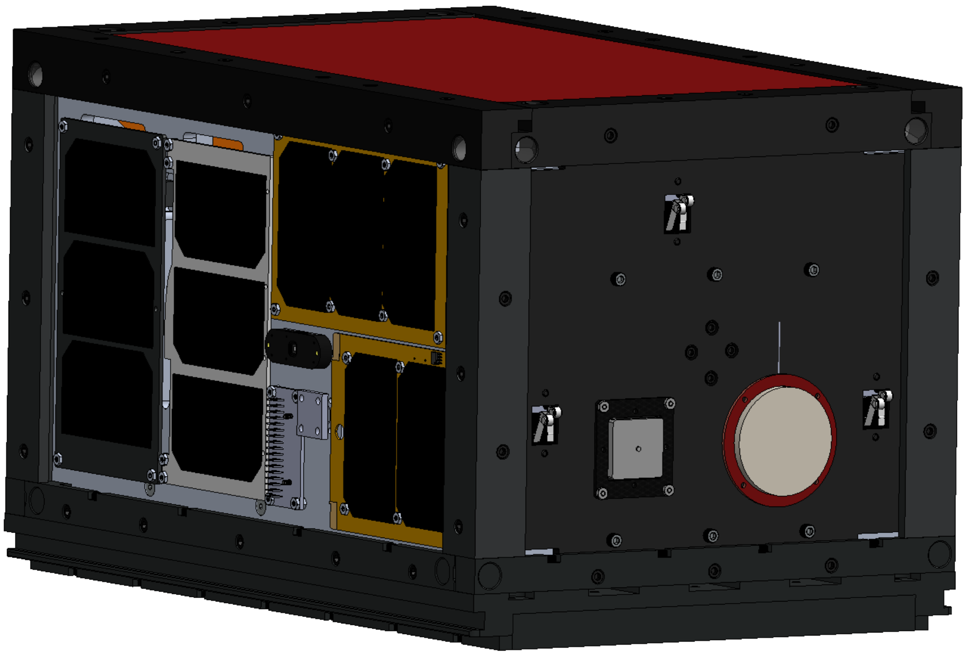

Figure 1. OrCa2 Assembled View.

The OrCa2 ADCS consists of a suite of sensors and a set of three custom-built magnetorquer actuators. An overview of this hardware is listed in Table 1. The GPS receiver, IMU, magnetometer, and magnetorquers will all be mounted internally on OrCa2, while the sun sensor will be mounted externally. An assembled view of the OrCa2 spacecraft is showed in Figure 1.

Table 1. OrCa2 ADCS Hardware Component List.

Hardware Type	Hardware	Manufacturer and Name	Quantity
Sensors	GPS Receiver	NearSpace Launch Eyestar	1
	Inertial Measurement Unit (IMU)	Epson M-G364[1]	1
	Magnetometer	Honeywell HMC1053[2]	1
	Fine Sun Sensor (FSS)	SolarMEMS nanoSSOC-D60[3]	1
Actuators	Magnetorquers	Custom	3

The lone sun sensor is mounted on the same external face as the 11 solar cells used to power the batteries of OrCa2, as is visible in Figure 1. This face will be controlled to point towards the sun in the sun pointing ADCS mode to maximize system power. The same control mode will also maximize the time during which the adjacent face in Figure 1containing the downlink antenna points above the horizon so that flight data can be retrieved from OrCa2. Calibration of the IMU and magnetometer will be performed prior to launch to minimize measurement error. The attitude control algorithm for simultaneous sun pointing and beacon pointing will be performed with the aid of Kalman filter-based attitude estimation. The detumble algorithm requires only magnetometer measurements and magnetorquer actuation and can be performed without the Kalman filter. The control algorithms for OrCa2 are explained in greater detail in the control algorithms section.

ADCS HARDWARE

This section will provide a brief overview of the architecture and function of the ADCS hardware components utilized by OrCa2.

IMU

The Epson M-G364 inertial measurement unit (IMU) provides both three-axis linear acceleration measurements within the range of ±3 G using an accelerometer and three-axis angular velocity measurements within the range of ±100 degrees per second using a gyroscope. The IMU interfaces with the on-board computer (OBC) through SPI communication protocol. 1 G is defined as 9.80665 m/s^2, which is the acceleration due to gravity at the Earth's surface. The IMU outputs accelerometer and gyro measurements in units of mG and degrees per second, respectively. For the purposes of Kalman filter attitude estimation, only the gyro measurements will be used. The IMU has an angular random walk parameter of 0.09 deg/hr$^{1/2}$, which characterizes the time rate of change of the gyro bias. The bias instability is 2.5 deg/hr and the gyro noise density is 0.002 deg/s/Hz$^{1/2}$. Gyro angular rate measurements will also be used in sun/beacon pointing control.

Magnetometer

A three-axis Honeywell HMC1053 magnetometer will be used by OrCa2 to measure the magnetic field throughout its orbit. Magnetic field measurements will be used for both the detumble controller and attitude estimation via the Kalman filter algorithm. This magnetometer is a sensitive, low field, solid-state analog sensor, the outputs of which are fed through an analog-to-digital converter (ADC), which interfaces with the OBC. The ADC outputs three voltages corresponding to the x, y, and z directions in the magnetometer reference frame. These voltages range from 0 to 3.3 V, which is the ADC reference voltage. The magnetic field measurements are converted to the spacecraft's body frame using a rotation matrix within the flight code.

Calibration of the magnetometer is necessary to adjust the raw measurements to account for both a constant offset from the true magnetic field and magnetic interference caused by other system components. The Engineering Sciences and Mechanics (ESM) building on Georgia Tech campus has a Helmholtz cage which can produce an artificial magnetic field. Outputs from the Honeywell magnetometer will be adjusted by comparing them to measurements from a second magnetometer at different external magnetic field values. The difference between the reference magnetometer and the Honeywell flight unit is a constant offset which can be added to all magnetometer measurements to remove bias.

Calibration also needs to take into account interference from other electronic components in the avionics stack as well as the magnetorquers, which significantly change the magnetic field in the vicinity of the magnetometer when they are turned on. To achieve this, magnetic field measurements were collected from the magnetometer over the range of magnetorquer currents for each of the three magnetorquers. Using these measured offsets, a lookup table was produced to compensate for the change in magnetic field when the magnetorquers are in use. This calibration prevents magnetorquer actuation from altering magnetometer measurements, which would decrease detumble controller and attitude estimation performance.

The magnetometer reads Earth's magnetic field in units of Gauss, so ADC voltage values must be converted back into Gauss to read sensor measurements. This conversion is performed using Eq. (1).

$$\boldsymbol{b}_G = \frac{\boldsymbol{V}_{ADC} - V_{ref}}{S V_{cc} G} \tag{1}$$

Table 2. Magnetometer Measurement Conversion Constants.

Constant	Value
G	413
V_{ref}	1.65 (V)
V_{cc}	3.3 (V)
S	0.001(Gauss^{-1})

The values for the constants used in the measurement conversion are listed in Table 2. In this relationship $\boldsymbol{b}_G$ is the vector magnetometer magnetic field measurement in units of Gauss, while $\boldsymbol{V}_{ADC}$ is the is the vector of ADC voltages obtained from the magnetometer output. The magnetometer circuit contains three voltage amplifiers which amplify the magnetometer outputs by a gain of G. V_{ref} is the reference voltage corresponding to a magnetic field of zero. V_{cc} is the magnetometer supply voltage. Voltages between zero and V_{ref} correspond to negative magnetic field vector components, while voltages between V_{ref} and V_{cc} correspond to positive components. S is the sensitivity of the magnetometer measurements which relates voltage changes to magnetic field changes, and it is listed in the magnetometer datasheet.

Sun Sensor

The SolarMEMS nanoSSOC-D60 is a two-axis sun sensor which measures both the azimuth and elevation of incident sun rays using four integrated silicon photodiodes. The sensor has a field of view defined by a view cone encompassing a range of ±60 degrees about the axis normal to the window through which sun rays travel into the interior and are detected by the photodiodes. The supply voltage to the sun sensor is 3.3 V like the magnetometer, and its measurements are 3σ accurate to within 0.5 degrees. This corresponds to a three-axis error standard deviation $\sigma_{s,3a}$ of approximately 0.167 degrees or a standard deviation σ_s of 0.0962 degrees per axis.

Azimuth and elevation angles are output by the sensor in degrees. A unit vector $\boldsymbol{s}$ corresponding to these two angles which points in the direction of the sun in the sensor reference frame can be computed using Eq. (2). This sun vector is transformed into the spacecraft body frame using a rotation matrix for use in the Kalman filter attitude estimation and sun pointing control.

$$\boldsymbol{s} = \frac{1}{\sqrt{tan^2(\alpha) + tan^2(\beta) + 1}} \begin{bmatrix} tan(\alpha) \\ tan(\beta) \\ 1 \end{bmatrix} \tag{2}$$

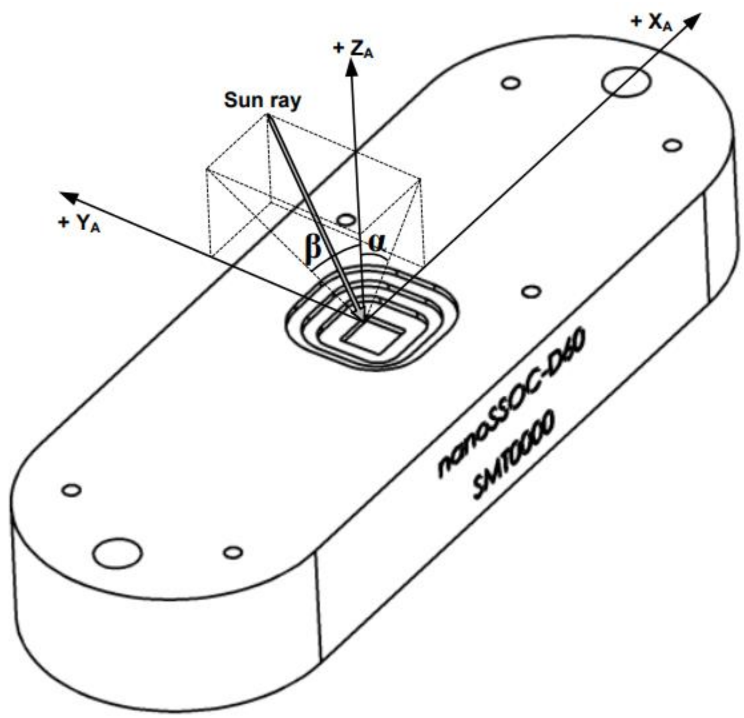

Figure 2. SolarMEMS Sun Sensor Body Frame.

Figure 2 shows the body frame of the sun sensor in which the sun direction azimuth and elevation angles are computed and in which the corresponding sun direction unit vector is based. The field of view requires that the sun be no more than 60 degrees away from the sensor z-axis for a sun vector to be measured. Because OrCa2 has only one of these sensors, it will be important to keep the external face housing the sun sensor and solar cells facing the sun not only for the power considerations of sun pointing but also to improve attitude estimation, which will rely entirely on gyro angular rates from the IMU and magnetometer data when sun pointing is not maintained to within 60 degrees.

Magnetorquers

Three custom magnetorquers were designed and manufactured in-house by the ADCS team for use on OrCa2. The magnetorquers are air coils rather than traditional cylindrical torque rods. The coils consist of copper wire looped around rectangular Garolite frames on each of the three spacecraft body axes. Running current through the wire produces a magnetic dipole moment which is used to exert a torque on the spacecraft in the presence of an external magnetic field. The theoretical magnetic dipole moment magnitude *m* produced by each air coil can be derived using the general formula in Eq. (3).

$$m = nIS \tag{3}$$

In this equation *n* is the number of loops of wire, *I* is the current run through the wire, and *S* is the rectangular area of each loop. Given that voltage is the product of current and resistance, the dipole moment magnitude can be rearranged into Eq. (4)[4].

$$m = n\frac{V}{R}S = n\frac{V}{\sigma nC}S = \frac{VS}{\sigma C} \tag{4}$$

In this relationship V is the same input voltage of 3.3 V as given to the OrCa2 sensors, σ is the electrical resistance per length of wire in ohms per meter, and C is the rectangular coil perimeter. It is worthy of note that the magnetic dipole moment based on this relation is not dependent on the number of coils of wire but instead on the coil area and perimeter.

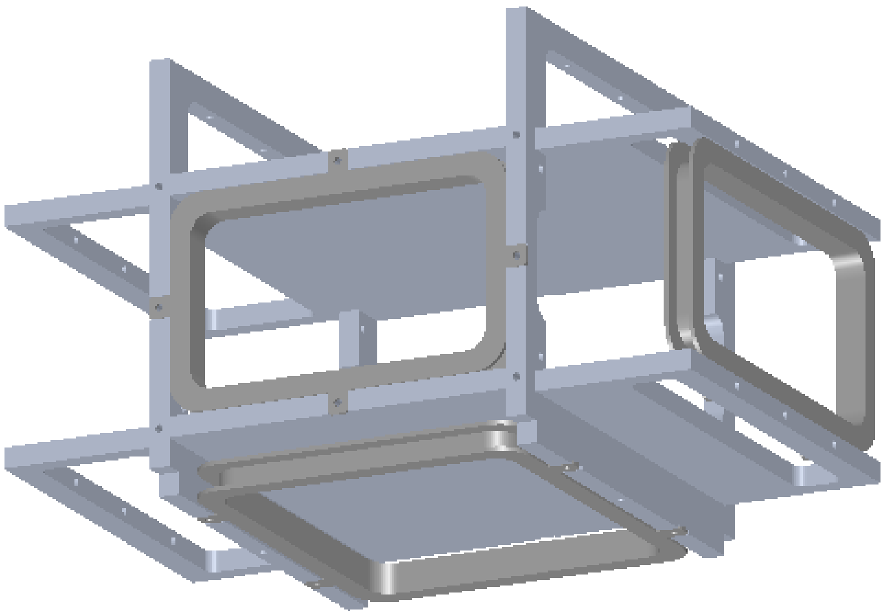

Figure 3. OrCa2 Support Structure and Air Coil Magnetorquer Geometry

Based on the 12U shape of OrCa2, the best way to maximize dipole moment is by utilizing the maximum feasible rectangular area on each axis. Figure 3 shows how this goal is achieved by maximizing coil area in each axis within the support structure, which houses the avionics stack.

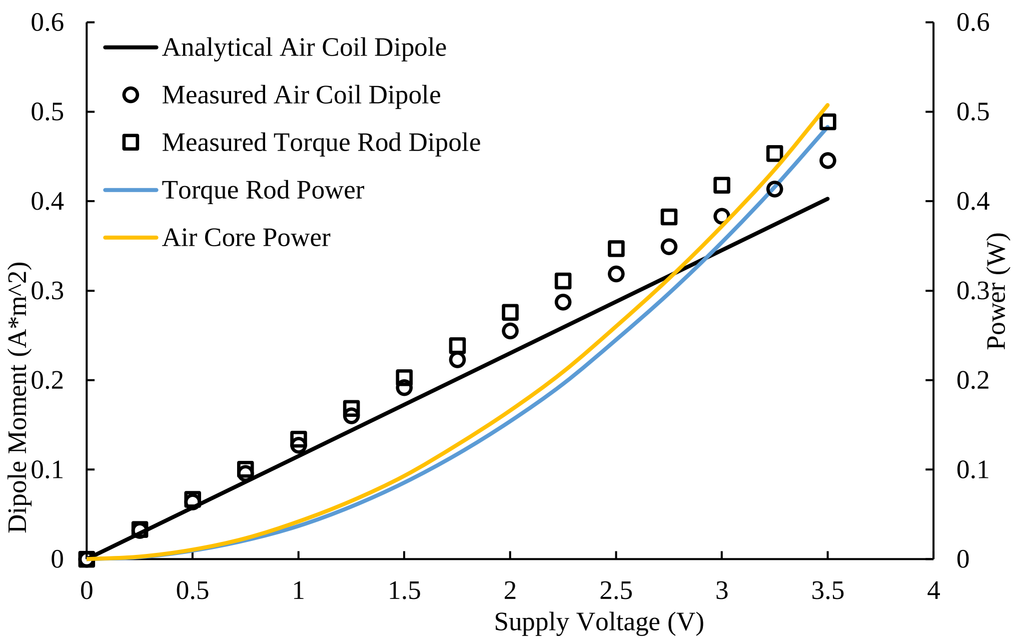

Figure 4. Air Coil Performance Relative to Analytical Formula and Torque Rods

Figure 4 summarizes the comparison between the air coils manufactured for OrCa2 and the traditional torque rod design of a coil wrapped around a ferromagnetic core. Power consumption and dipole moments were measured over a range of supply voltages for both an air coil and a comparable torque rod designed for the TARGIT CubeSat mission. The comparison shows that for a given input voltage the air coils produce a slightly lower dipole moment and consume slightly more power, but the difference is marginal. The measured air coil dipole moment also compares favorably to the analytical estimate from Eq. (4).

Because coil dipole moments are theoretically constrained only by input voltage, resistance properties of the wire, and coil geometry, the number of loops n was designed with current and power considerations in mind. The wire used for the air coils is 30 AWG insulated copper wire, which has an approximate resistance σ of 0.338496 Ohms per meter and an upper limit of current for power transmission (I_{max}) of 0.142 Amps[*]. From these values it is possible to back out a minimum number of loops n_{min} for each air coil using Eq. (5-7).

$$R_{min} = \sigma L_{min} = \frac{V_{cc}}{I_{max}} \tag{5}$$

$$L_{min} = n_{min} C \geq \frac{V_{cc}}{\sigma I_{max}} \tag{6}$$

$$n_{min} \geq \frac{V_{cc}}{C \sigma I_{max}} \tag{7}$$

Table 3. OrCa2 Air Coil Magnetorquer Wire Loop Counts.

Small Coil	Medium Coil	Large Coil
213	200	156

Each air coil was wrapped with enough wire to correspond to a total wire resistance of approximately 33.5 Ohms, which corresponds to a current of 0.0985 Amps. The number of loops for each coil on the flight unit is listed in Table 3. This increase above the minimum loop count results in a reduction of approximately 30.6% from the upper current limit, and consequently power consumption is reduced by this same percentage. The flight unit air coils will draw approximately 325 mW of power each.

ADCS CONTROL ALGORITHMS

The OrCa2 ADCS relies on both attitude estimation using an extended Kalman filter (EKF) and two separate attitude control modes for attitude adjustment. One control mode handles detumbling, while the other maximizes beaconing time while maintaining sun pointing for maximum power generation. The algorithms driving each of these components are discussed separately below.

Detumble Control

Deployment in orbit will result in an initial, random tumbling angular velocity for the OrCa2 CubeSat. The first task of the ADCS will be to detumble the spacecraft to remove this initial spin

[*] https://www.powerstream.com/Wire_Size.htm

and bring the attitude to a steady state. The algorithm used for detumble on OrCa2 is a simple "B-dot" controller which requires only magnetometer measurements and magnetorquer actuation. This choice of controller was made deliberately so that OrCa2 can detumble even if the Kalman filter-based attitude estimation, which requires more power and sensor data, has failed.

The B-dot controller functions by measuring the change in magnetic field readings measured by the magnetometer between two consecutive time steps and actuating the magnetorquers to produce a dipole moment opposing this change. The change in magnetic field divided by the time step between measurements is denoted as $\dot{\boldsymbol{b}}$. To reduce the impact of magnetometer measurement noise on the performance of this controller, a moving average of 10 measurements is used to smooth the raw output data. The commanded dipole moment $\boldsymbol{m}$ is computed by the controller using Eq. (8) and Eq. (9), where k is the controller gain. This gain was adjusted experimentally to optimize performance at the expected random tumble rates on orbit, as discussed below in the testing section.

$$\dot{\boldsymbol{b}} = \frac{\boldsymbol{b}_k - \boldsymbol{b}_{k-1}}{\Delta t} \tag{8}$$

$$\boldsymbol{m} = -k\dot{\boldsymbol{b}} \tag{9}$$

Sun Pointing and Beacon Pointing Control

The optimal pointing scheme for OrCa2 after detumbling is to point the body axis corresponding to the sun sensor and solar panel face directly in the sun-pointing direction $\boldsymbol{r}_{s,I}$. At the same time, the orthogonal downlink antenna boresight axis will point towards the projection of the orbit eccentricity vector $\boldsymbol{e}$ onto the plane orthogonal to $\boldsymbol{r}_{s,I}$. This pointing scheme keeps the sun sensor and solar panels constantly normal to the sun while also maximizing downlink beacon time by keeping the downlink antenna pointed above the horizon.

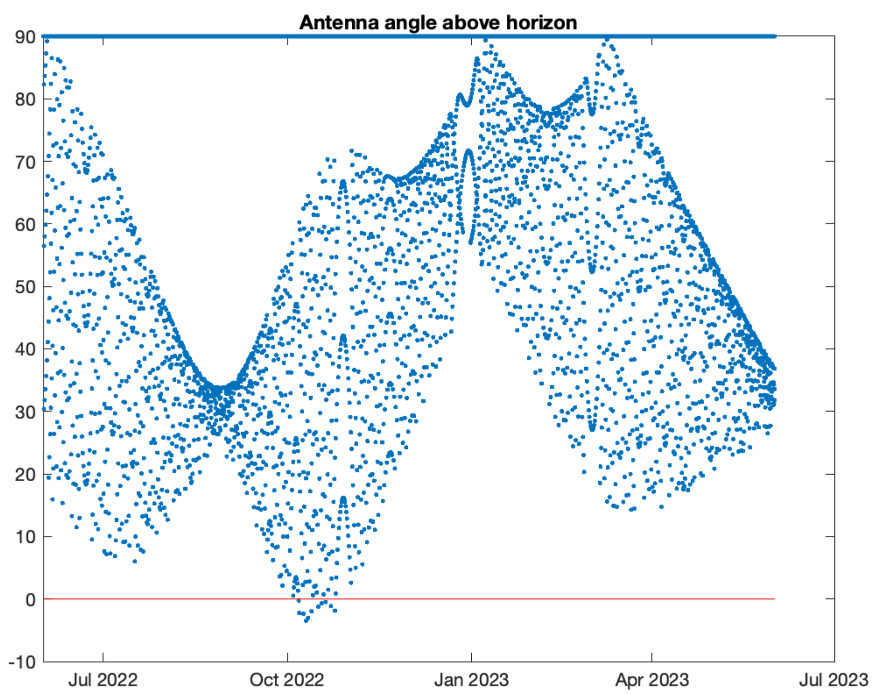

Figure 5. OrCa2 Downlink Antenna Zenith Pointing Performance.

The projected downlink antenna angles above the horizon for the OrCa2 mission are plotted in Figure 5. These results show that the pointing scheme described above successfully maintains an attitude with the downlink antenna pointing above the horizon for almost the entire mission, allowing for data beacons through the Iridium satellite constellation. For orbital altitudes below the Iridium constellation, the downlink antenna maintains an average attitude of 46 degrees above the horizon, leaving a sizeable margin of error.

The eccentricity vector, which points from the orbit apoapsis towards its periapsis, is computed in Eq. (11) using the angular momentum $\boldsymbol{h}$ in Eq. (10). The standard gravitational parameter μ of Earth is approximately 3.986×10^5 kg^3/s^2.

$$\boldsymbol{h} = \boldsymbol{r_{s,I}} \times \boldsymbol{v_{s,I}} \tag{10}$$

$$\boldsymbol{e} = \frac{\boldsymbol{v_{s,I}} \times \boldsymbol{h}}{\mu} - \frac{\boldsymbol{r_{s,I}}}{\|\boldsymbol{r_{s,I}}\|} \tag{11}$$

The projection of $\boldsymbol{e}$ onto the plane orthogonal to the sun direction unit vector $\boldsymbol{r}_{s,I}$.is given by $\boldsymbol{z_{proj}}$ in Eq. (12). The rotation matrix $\boldsymbol{A_{point}}$ in Eq. (13) describes the desired attitude such that the spacecraft body frame aligns with the desired sun and beacon pointing directions.

$$\boldsymbol{z_{proj}} = \boldsymbol{e} - (\boldsymbol{e} \cdot \boldsymbol{r_{s,I}})\boldsymbol{r_{s,I}} \tag{12}$$

$$\boldsymbol{A_{point}} = \left[(\boldsymbol{z_{proj}} \times \boldsymbol{r}_{s,I}) \quad -\boldsymbol{r}_{s,I} \quad -\boldsymbol{z_{proj}}\right] \tag{13}$$

The sun and beacon pointing scheme is implemented on OrCa2 using a PD attitude quaternion feedback controller. A reference quaternion $\boldsymbol{q}_{ref}$ corresponding to the desired attitude is constructed at each time step using the attitude rotation matrix $\boldsymbol{A_{point}}$ defined in Eq. (13). An error quaternion $\boldsymbol{\delta q}$ between the desired reference attitude and the current Kalman filter estimated attitude $\hat{\boldsymbol{q}}$ is constructed using the quaternion tensor product in Eq. (14).

$$\boldsymbol{\delta q} = \begin{bmatrix} \boldsymbol{\delta q}_{1:3} \\ \delta q_4 \end{bmatrix} = \hat{\boldsymbol{q}} \otimes \boldsymbol{q}^*_{ref} \tag{14}$$

The PD control law in Eq. (15) is then used to compute a desired torque $\boldsymbol{\tau}$, which is executed by the magnetorquers using the cross product. relationship between torque, dipole moment, and magnetic field vector $\boldsymbol{B}$ in Eq. (17). J represents the inertia tensor of the OrCa2 spacecraft. The sign term in the proportional part of the control law ensures that the controller takes the shorter route to the desired pointing attitude.

$$\boldsymbol{\tau} = -k_p \boldsymbol{sign}(\delta q_4)\boldsymbol{\delta q}_{1:3} - k_d\hat{\boldsymbol{\omega}} - [\hat{\boldsymbol{\omega}} \times]J\hat{\boldsymbol{\omega}} \tag{15}$$

$$[\hat{\boldsymbol{\omega}} \times] = \begin{bmatrix} \mathbf{0} & -\hat{\boldsymbol{\omega}}_{\boldsymbol{z}} & \hat{\boldsymbol{\omega}}_{\boldsymbol{y}} \\ \hat{\boldsymbol{\omega}}_{\boldsymbol{z}} & \mathbf{0} & -\hat{\boldsymbol{\omega}}_{\boldsymbol{x}} \\ -\hat{\boldsymbol{\omega}}_{\boldsymbol{y}} & \hat{\boldsymbol{\omega}}_{\boldsymbol{x}} & \mathbf{0} \end{bmatrix} \tag{16}$$

$$\boldsymbol{m} = \boldsymbol{B} \times \boldsymbol{\tau} \tag{17}$$

The proportional and derivative gains in this controller k_p and k_d are implemented as functions of desired controller bandwidth ω_n and damping ratio ζ as detailed in Eq. (18) and Eq. (19).

$$k_p = \omega_n^2 J \tag{18}$$

$$k_d = 2\zeta\omega_n J \tag{19}$$

EXTENDED KALMAN FILTER

Unlike the detumble mode, the sun-pointing and beaconing control mode requires knowledge of OrCa2's attitude. Attitude estimation is achieved by processing magnetometer, IMU, and sun sensor measurements using the "mission mode" multiplicative EKF derived in section 6.2.4 of *Fundamentals of Spacecraft Attitude Determination and Control* by Markley and Crassidis[5]. This filter estimates both attitude and gyro bias using a state vector consisting of a small angle rotation vector and a change in bias as seen in in Eq. (20). Note that this state represents a deviation from the attitude and bias of the previous step and not the attitude and bias themselves, so the state is initialized as zero and reset to zero after each measurement update.

$$\Delta \boldsymbol{x} = \begin{bmatrix} \delta\boldsymbol{\theta} \\ \Delta\boldsymbol{\beta} \end{bmatrix} \tag{20}$$

Time Update

The EKF used by OrCa2 consists of a time update in which the state and state error covariance are propagated from one time step to the next using IMU gyro measurements and a measurement update in which magnetometer and sun sensor measurements are used to update the state estimate and error covariance. During the time update, the attitude estimate is propagated using the gyro measurements adjusted for the current bias estimate. At the current time step k, the angular rate estimate $\widehat{\boldsymbol{\omega}}_k^+$ is computed by subtracting the estimated bias $\widehat{\boldsymbol{\beta}}_k$ from the measured gyro rates $\boldsymbol{\omega}_{meas,k}$ as showed in Eq. (21). The bias is assumed to be zero upon initialization of the filter.

$$\widehat{\boldsymbol{\omega}}_k^+ = \boldsymbol{\omega}_{meas,k} - \widehat{\boldsymbol{\beta}}_k \tag{21}$$

The attitude quaternion estimate is propagated to the next time step using the discrete time propagation matrix $\theta(\widehat{\boldsymbol{\omega}}_k^+)$ given in Eq. (22), where Δt represents the filter sample rate.

$$\widehat{\boldsymbol{q}}_{k+1}^- = \theta(\widehat{\boldsymbol{\omega}}_k^+)\widehat{\boldsymbol{q}}_k^+ \tag{22}$$

$$\theta(\widehat{\boldsymbol{\omega}}_k^+) = \begin{bmatrix} cos\left(\frac{1}{2}\|\widehat{\boldsymbol{\omega}}_k^+\|\Delta t\right) I_3 - \left[\widehat{\boldsymbol{\Psi}}_{\boldsymbol{k}}^+ \times\right] & \widehat{\boldsymbol{\Psi}}_{\boldsymbol{k}}^+ \\ -\left(\widehat{\boldsymbol{\Psi}}_{\boldsymbol{k}}^+\right)^{\boldsymbol{T}} & cos\left(\frac{1}{2}\|\widehat{\boldsymbol{\omega}}_k^+\|\Delta t\right) \end{bmatrix} \tag{23}$$

$$\widehat{\boldsymbol{\Psi}}_{\boldsymbol{k}}^+ = \frac{sin\left(\frac{1}{2}\|\widehat{\boldsymbol{\omega}}_k^+\|\Delta t\right)\widehat{\boldsymbol{\omega}}_k^+}{\|\widehat{\boldsymbol{\omega}}_k^+\|} \tag{24}$$

The error covariance of the state vector is propagated to the next time step using the discrete error-state transition matrix Φ_k defined in Eq. (25-27) and the process noise matrices Q_k and Y_k defined in Eq. (28). The process noise depends on both the gyro measurement white noise standard deviation σ_v and the bias random walk parameter σ_u, which were discussed in the IMU section.

$$\Phi_\mathrm{k} = \begin{bmatrix} \Phi_{11} & \Phi_{12} \\ 0_{3\times3} & I_3 \end{bmatrix} \tag{25}$$

$$\Phi_{11} = I_3 - [\widehat{\boldsymbol{\omega}}_k^+ \times]\frac{sin(\|\widehat{\boldsymbol{\omega}}_k^+\|\Delta t)}{\|\widehat{\boldsymbol{\omega}}_k^+\|} + [\widehat{\boldsymbol{\omega}}_k^+ \times]^2\frac{1 - cos(\|\widehat{\boldsymbol{\omega}}_k^+\|\Delta t)}{\|\widehat{\boldsymbol{\omega}}_k^+\|^2} \tag{26}$$

$$\Phi_{22} = [\widehat{\boldsymbol{\omega}}_k^+ \times]\frac{1 - cos(\|\widehat{\boldsymbol{\omega}}_k^+\|\Delta t)}{\|\widehat{\boldsymbol{\omega}}_k^+\|^2} - I_3\Delta t - [\widehat{\boldsymbol{\omega}}_k^+ \times]^2\frac{\|\widehat{\boldsymbol{\omega}}_k^+\|\Delta t - sin(\|\widehat{\boldsymbol{\omega}}_k^+\|\Delta t)}{\|\widehat{\boldsymbol{\omega}}_k^+\|^3} \tag{27}$$

$$Q_k = \begin{bmatrix} \left(\sigma_v^2\Delta t + \frac{1}{3}\sigma_u^2\Delta t^3\right) I_3 & -\left(\frac{1}{2}\sigma_u^2\Delta t^2\right) I_3 \\ -\left(\frac{1}{2}\sigma_u^2\Delta t^2\right) I_3 & (\sigma_u^2\Delta t) I_3 \end{bmatrix}, \qquad Y_k = I_6 \tag{28}$$

The error-state transition matrix and process noise are used to propagate covariance from time step k to time step k+1 as detailed in Eq. (29).

$$P_{k+1}^- = \Phi_k P_k^+ \Phi_k^T + Y_k Q_k Y_k^T \tag{29}$$

Measurement Update

Once the state and covariance are propagated from one step to the next, the filter processes the magnetometer and sun sensor measurements at the new time step and computes an optimal Kalman gain based on the expected measurements and measurement error covariance. The gain is then used along with the difference between the true and expected measurements to update the error state vector and covariance. The new state vector is used to update both the attitude quaternion estimate and the gyro bias estimate. The measurement vector $\boldsymbol{y}_k$ in Eq. (30) consists of both the magnetic field vector measurement $\boldsymbol{b}_m$ from the magnetometer and the sun vector measurement $\boldsymbol{b}_s$from the sun sensor. Both measurements are smoothed within the filter algorithm using a 10-measurement moving average to reduce the impact of noise and improve estimation performance.

$$\boldsymbol{y}_k = \begin{bmatrix} \boldsymbol{b}_m \\ \boldsymbol{b}_s \end{bmatrix} \tag{30}$$

The expected magnetic field and sun vector measurements are computed by rotating the known inertial magnetic field vector $\boldsymbol{r}_{m,I}$ and inertial sun pointing vector $\boldsymbol{r}_{s,I}$ into the body frame. The inertial magnetic field vector is determined using the International Geomagnetic Reference Field (IGRF) model, which is implemented in the flight software[6]. The inertial sun pointing vector is computed by subtracting the current inertial spacecraft position from the current inertial sun position $\boldsymbol{p}_{s,I}$, which is pulled from an ephemeris stored onboard the flight computer, using Eq. (31). Note that both inertial vectors require the position of OrCa2 to compute. This reliance on position data for attitude estimation makes consistent GPS positioning important for ADCS mission objectives.

$$\boldsymbol{r}_{s,I} = \left(\boldsymbol{p}_{s,I} - \boldsymbol{r}_I\right) / \left\|\boldsymbol{p}_{s,I} - \boldsymbol{r}_I\right\| \tag{31}$$

The current vector of expected measurements $\boldsymbol{h}_k(\hat{\boldsymbol{x}}_k^-)$ in Eq. (32) is constructed by rotating the inertial measurement vectors into the body frame using a rotation matrix $A(\hat{\boldsymbol{q}}_k^-)$ derived from the most recent attitude quaternion estimate. Eq. (33) shows how this rotation matrix is derived from the estimated attitude quaternion elements.

$$\boldsymbol{h}_k(\hat{\boldsymbol{x}}_k^-) = \begin{bmatrix} A(\hat{\boldsymbol{q}}_k^-)\boldsymbol{r}_{m,I} \\ A(\hat{\boldsymbol{q}}_k^-)\boldsymbol{r}_{s,I} \end{bmatrix} \tag{32}$$

$$A(\hat{\boldsymbol{q}}_k^-) = \begin{bmatrix} q_1^2 - q_2^2 - q_3^2 + q_4^2 & 2(q_1q_2 + q_3q_4) & 2(q_1q_3 - q_2q_4) \\ 2(q_2q_1 - q_3q_4) & -q_1^2 + q_2^2 - q_3^2 + q_4^2 & 2(q_2q_3 + q_1q_4) \\ 2(q_3q_1 + q_2q_4) & 2(q_3q_2 - q_1q_4) & -q_1^2 - q_2^2 + q_3^2 + q_4^2 \end{bmatrix} \tag{33}$$

The measurement sensitivity matrix relates the measurements to the state vector. Magnetometer and sun sensor measurements are related to the attitude but are independent of the gyro bias, which is why the right half of the sensitivity matrix in Eq. (34) is zero.

$$H_k(\hat{\boldsymbol{x}}_k^-) = \begin{bmatrix} [A(\hat{\boldsymbol{q}}_k^-)\boldsymbol{r}_{m,I}\times] & 0_{3\times3} \\ [A(\hat{\boldsymbol{q}}_k^-)\boldsymbol{r}_{s,I}\times] & 0_{3\times3} \end{bmatrix} \tag{34}$$

Computing the Kalman gain also requires the measurement error covariance matrix in Eq. (35). This matrix is time invariant and depends only upon the standard deviation of magnetometer and sun vector errors, which are given by σ_m and σ_s, respectively. If the sun is not visible to the sun sensor, the invalid sun vector measurement can be effectively ignored by the filter by setting σ_s to an extremely large number. Given all of the required components, the Kalman K_k gain is computed using Eq. (36).

$$R_k = \begin{bmatrix} \sigma_m^2 I_3 & 0_{3\times3} \\ 0_{3\times3} & \sigma_s^2 I_3 \end{bmatrix} \tag{35}$$

$$K_k = P_k^- H_k^T(\hat{\boldsymbol{x}}_k^-)\left[H_k(\hat{\boldsymbol{x}}_k^-)P_k^- H_k^T(\hat{\boldsymbol{x}}_k^-) + R_k\right]^{-1} \tag{36}$$

The measurement update to the state vector uses both the Kalman gain and the difference between observed and expected measurements as detailed in Eq. (37). The state error covariance P_k is updated according to Eq. (38).

$$\Delta\hat{\boldsymbol{x}}_k^+ = \begin{bmatrix} \delta\hat{\boldsymbol{\theta}}_{\boldsymbol{k}}^+ \\ \Delta\hat{\boldsymbol{\beta}}_{\boldsymbol{k}}^+ \end{bmatrix} = K_k[\boldsymbol{y}_k - \boldsymbol{h}_k(\hat{\boldsymbol{x}}_k^-)] \tag{37}$$

$$P_k^+ = [I_3 - K_k H_k(\hat{\boldsymbol{x}}_k^-)]P_k^- \tag{38}$$

Attitude and Bias Estimate Update

Because the state vector consists of only a deviation from the attitude and gyro bias and not these quantities themselves, an extra step is required to update the attitude quaternion and bias vector estimates. Using the rotation vector portion $\delta\hat{\boldsymbol{\theta}}_{\boldsymbol{k}}^+$ of the error state $\Delta\hat{\boldsymbol{x}}_k^+$ taken from the measurement update output, the attitude quaternion estimate $\hat{\boldsymbol{q}}_k$ is updated using Eq. (39-41). Because Eq. (39) is an additive update, Eq. (41) is needed to conform to the restraint that an attitude quaternion must have unity magnitude. The error introduced by this normalization is minimal so long as the rotation vector consists of small angles.

$$\boldsymbol{q}_k^* = \hat{\boldsymbol{q}}_k^- + \frac{\mathbf{1}}{\mathbf{2}}\boldsymbol{\Xi}(\hat{\boldsymbol{q}}_k^-)\delta\hat{\boldsymbol{\theta}}_{\boldsymbol{k}}^+ \tag{39}$$

$$\boldsymbol{\Xi}(\hat{\boldsymbol{q}}_k^-) = \begin{bmatrix} q_4 & -q_3 & q_2 \\ q_3 & q_4 & -q_1 \\ -q_2 & q_1 & q_4 \\ -q_1 & -q_2 & -q_3 \end{bmatrix} \tag{40}$$

$$\hat{\boldsymbol{q}}_k^+ = \frac{\boldsymbol{q}_k^*}{\|\boldsymbol{q}_k^*\|} \tag{41}$$

The gyro bias estimate is updated by adding the estimate for the change in bias $\Delta\hat{\boldsymbol{\beta}}_{\boldsymbol{k}}^+$ from the measurement update output to the bias estimate from the previous step using Eq. (42). The bias estimate is initialized as zero before running the filter.

$$\hat{\boldsymbol{\beta}}_{\boldsymbol{k}}^+ = \hat{\boldsymbol{\beta}}_{\boldsymbol{k}}^- + \Delta\hat{\boldsymbol{\beta}}_{\boldsymbol{k}}^+ \tag{42}$$

After the attitude and bias estimates have been updated using the state deviation vector, it is reset to zero to reflect that the current attitude and bias estimates represent the new nominal trajectory. The attitude and bias are repeatedly updated as new sensor measurements are processed.

TESTS

Testing of the OrCa2 ADCS algorithms was performed on the engineering unit using the air bearing and Helmholtz cage setup in the ESM G6 lab on Georgia Tech campus.

Detumble

To test the detumble control algorithm, the engineering unit was placed on the air bearing and given an initial spin. Angular rates were measured during the test using the IMU, and detumble controller outputs were recorded. The air bearing and the Helmholtz cage were designed for smaller CubeSats, and perfectly balancing the engineering unit on the air bearing proved difficult. The engineering unit was extremely sensitive to minute changes in the test stand center of mass, which caused the unit to oscillate about the vertical axis when left still.

To adjust for this perturbation and the deceleration effects of friction and drag on the engineering unit, two separate tests were performed. In the first test, the detumble controller was turned on. In the second (control) test, the engineering unit was left to spin uncontrolled. An estimate of effective detumble controller acceleration was determined by comparing the detumble test to the control test. In order to ensure the validity of the comparison between these tests, it was necessary to perform both tests on the same day with the same balance offset on the air bearing.

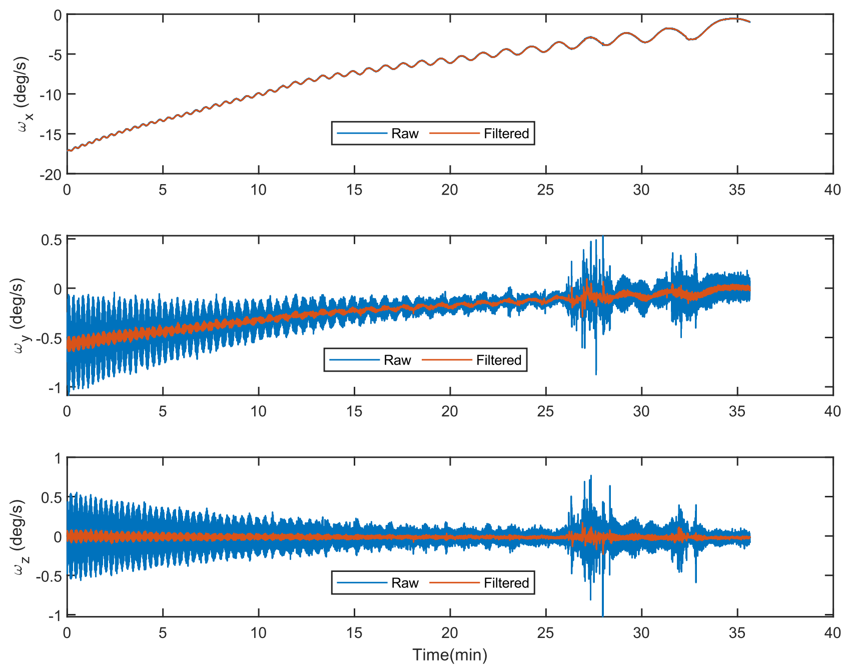

Figure 6. Detumble Test 3-Axis Angular Rates.

Figure 6 shows an example of the both the raw angular rate measurements and the filtered 10-measurement moving average rates during a detumble test. The engineering unit oscillated mainly about the x-axis, which is the air bearing axis of rotation, but smaller oscillations were also present in the other axes. This test shows the utility of filtering the angular rate measurements, especially at low spin rates, to minimize extra controller actuation due to measurement noise. The periodic character of the angular rates is caused by the engineering unit mass imbalance on the test stand.

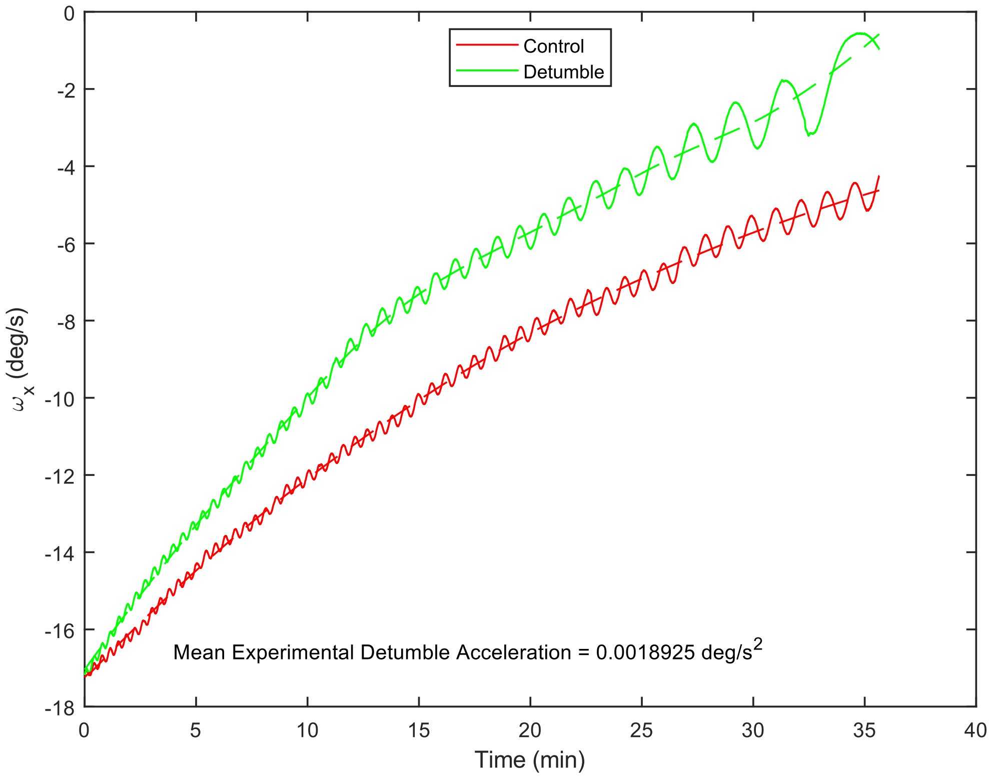

Figure 7. Detumble Test Angular Rate Comparison.

Figure 7 compares the filtered angular rates about the x-axis between the detumble and control tests starting from the same initial angular rate. It is evident that the detumble controller achieves a higher rate of angular deceleration than is present in the control test. Smoothing the rates to remove the periodic oscillation and comparing the two final angular rates yields a detumble controller differential angular acceleration $\dot{\omega}_{detumble}$ of approximately 0.0018935 deg/s using Eq. (43).

$$\dot{\omega}_{detumble} = \frac{\omega_{x,detumble}^{final} - \omega_{x,control}^{final}}{t_{test}} \tag{43}$$

Assuming that this detumble controller acceleration is roughly constant, a random tumble of 10 deg/s could be eliminated in approximately 88 minutes of controller actuation. Because OrCa2 will have a geostationary transfer orbit (GTO) and spend most of this orbit outside the useful range of the Earth's magnetic field, a full detumble from this initial angular rate would likely require multiple orbits to complete.

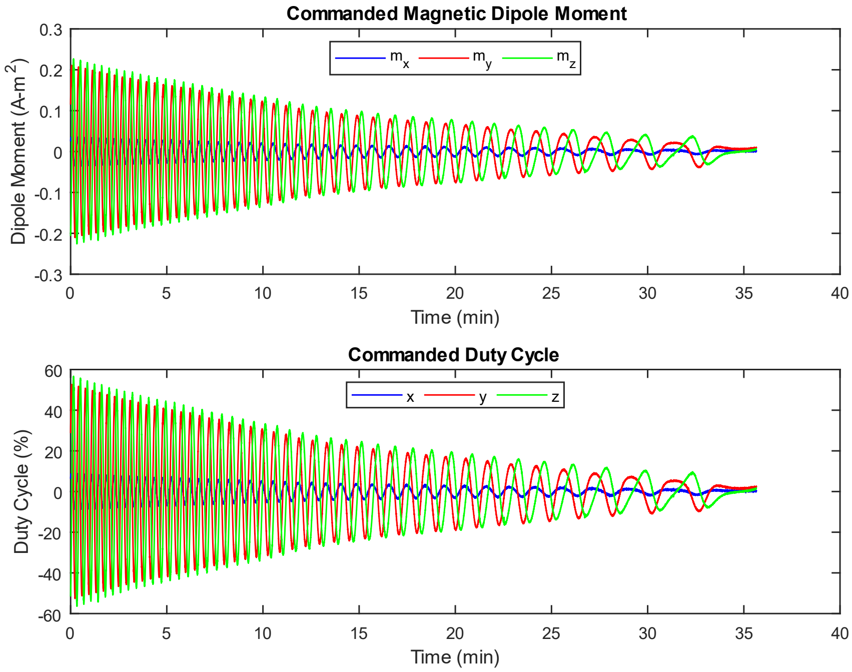

Figure 8. Detumble Controller Commanded Dipole Moments and Duty Cycles.

Figure 8 plots the magnetic dipole moments and corresponding duty cycles commanded to each air coil by the detumble controller during the test. These quantities are directly proportional because the duty cycle corresponds to the current supply given to each coil. The duty cycles during this test had a mean magnitude $\overline{D}$ of 30.01% and did not approach the maximum of 100 even at a spin rate of about 17 deg/s, which is likely higher than any rate OrCa2 will experience on orbit. To maximize magnetorquer actuation at tumble rates greater than a few degrees per second, the controller gain was multiplied by 30 compared to the gain used in the test described above. This gain increase will result in a higher rate of deceleration from the detumble controller.

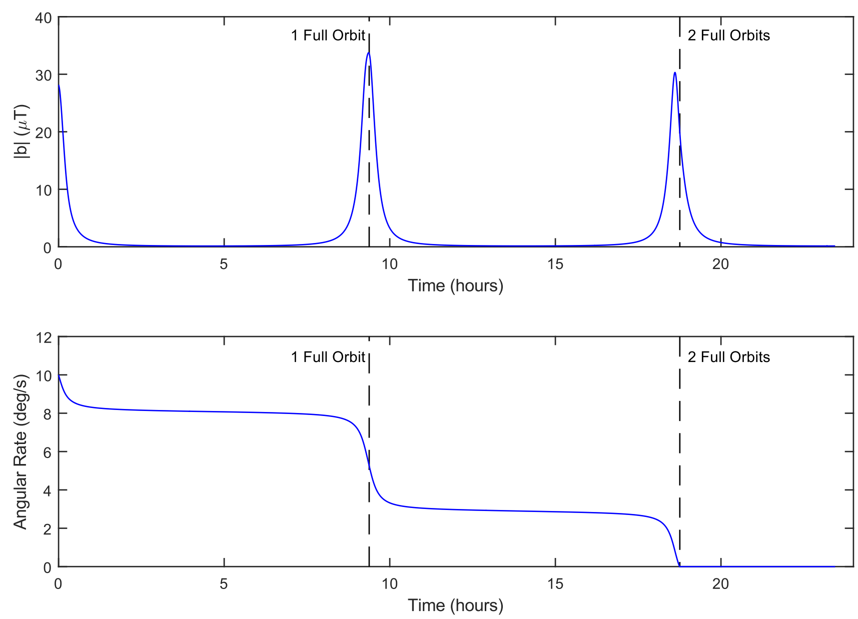

Figure 9. OrCa2 Magnetic Field and Detumble Simulation

Figure 9 shows the profile of the magnetic field magnitude for OrCa2 over multiple orbits based on the IGRF model. The magnetic field magnitudes are significant for a brief window during each orbit due to the GTO shape, and they never approach the higher average magnetic field b_{test} produced during the lab detumble test using the Helmholtz cage, which had a magnitude of 77.2 μT. The second half of Figure 9 shows the simulated angular rate ω of OrCa2 during detumble over time assuming conservatively that the duty cycle does not exceed 75%. Eq. (44) shows how the estimated detumble acceleration from the lab test was scaled to match conditions on orbit.

$$\dot{\omega} = \frac{\|b\|}{\|b_{test}\|}\frac{75\%}{\overline{D}}\dot{\omega}_{detumble} \tag{44}$$

This analysis assumes that the moment of inertia about the random tumbling axis matches the moment of inertia of the engineering unit and test stand about the vertical axis during air bearing testing, but the extra weight added by the test stand makes this a reasonable assumption. The integration of expected angular accelerations from the detumble controller shows that OrCa2 is predicted to be able to fully detumble from a 10 deg/s initial angular rate within two orbits.

Kalman Filter and Pointing Controller

The EKF and sun/beacon pointing controller were tested using a halogen lamp in the lab to simulate the sun. For the purposes of testing, the inertial sun position was set equal to the body-frame sun vector measurement from the sun sensor when the sun sensor face of the engineering unit pointed directly towards the lamp. This arrangement corresponds toa unity attitude quaternion ($\boldsymbol{q}_{1:3} = 0_{3\times 1},\ q_4 = 1$) when the sun sensor points towards the lamp.

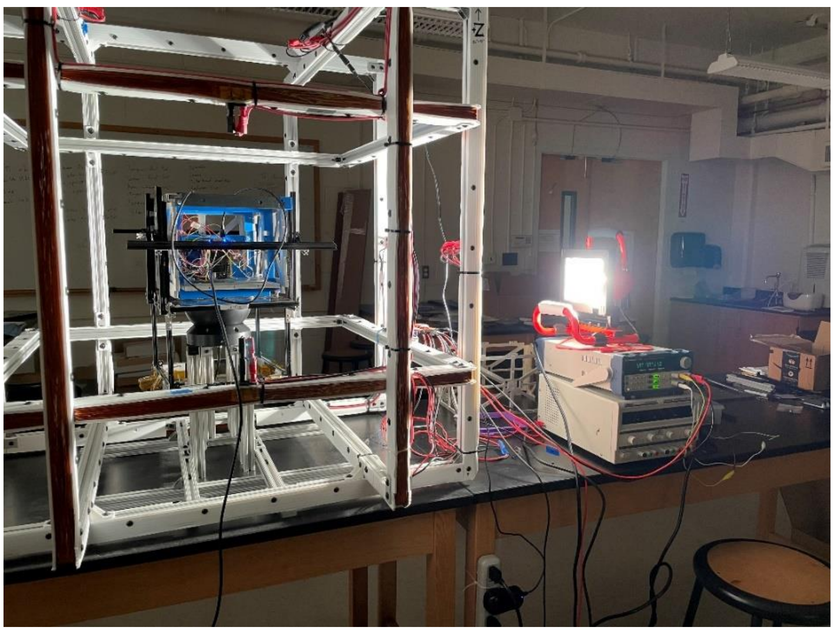

Figure 10. Engineering Unit Air Bearing Setup.

The lab setup for Kalman filter and pointing control testing is showed in Figure 10. The engineering unit was rotated to a small offset angle about the negative vertical (x) axis and then left to rotate with the sun pointing controller turned on. The magnetorquers were unable to overcome the disturbance torque of the engineering unit center of gravity offset, but the EKF outputs and controller commands show that the pointing controller produced torques in the correct direction to achieve sun pointing.

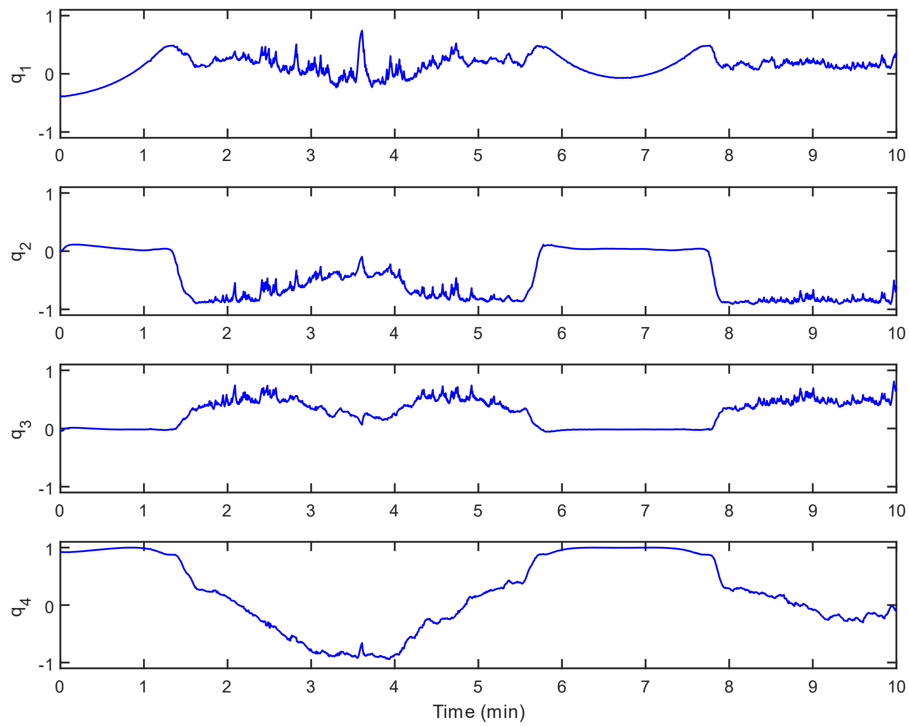

Figure 11. EKF Attitude Quaternion Element Estimates.

The EKF attitude quaternion estimates from a sun pointing test are plotted in Figure 11. The EKF correctly determined that the engineering unit began at an attitude rotated about the negative x-axis relative to the reference sun-pointing position and then rotated in the positive x direction past the sun direction. Because the magnetorquers were weaker than the disturbance torque, the engineering unit continued to rotate until the lamp was outside of the 60-degree sun sensor field of view. This point corresponds to the sudden deviation in quaternion estimates around the 1 minute and 30 second mark.

The engineering unit continued rotating then slowed down and changed directions due to the center of gravity offset while the sun sensor faced away from the lamp. It rotated back towards the lamp about the negative x-axis, and the sun sensor began to read valid sun vector directions again approximately 5 minutes and 40 seconds into the test. The engineering unit rotated until it passed the sun pointing direction by a small offset then changed directions again due to the center of gravity offset, rotating back in the positive x-axis direction for the remainder of the test. After a 60-degree offset the sun sensor lost contact with the lamp for a second time, causing a second sudden deviation in EKF quaternion estimates. The EKF outputs from this test show that the filter attitude estimates match expectations when the sun is visible to the sun sensor but deviate significantly when the sun is outside the sensor field of view.

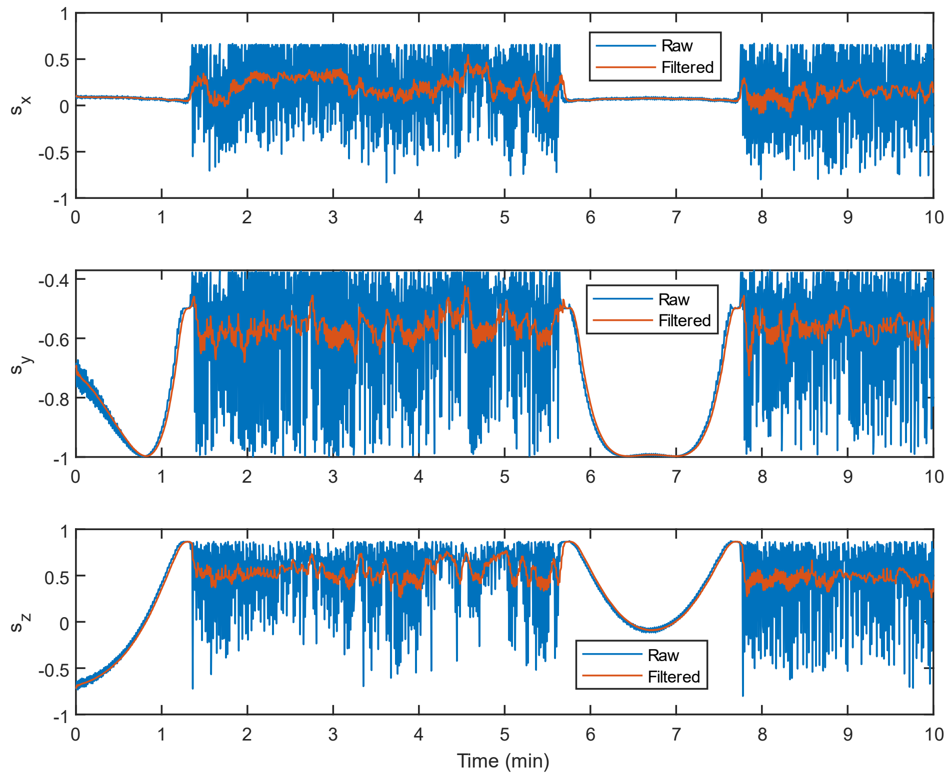

Figure 12. Sun Sensor Measurement Vector Components.

Figure 12, which plots the components of the sun vector measurements during the same test, explains the inability of the EKF to accurately track the engineering unit attitude while pointed away from the lamp. When the lamp is outside the sun sensor field of view the sun vector oscillates wildly, feeding incorrect measurements into the EKF measurement model.

The solution to this problem is to ignore the sun sensor measurements when OrCa2 is not sun pointing by setting the measurement error covariance to an arbitrarily high number as discussed in the EKF section. This allows the EKF to estimate attitude based only on the magnetometer measurements, which do not depend on sun pointing. Because the magnetic field weakens at higher orbital altitudes, consistent sun pointing is desirable to maintain accurate attitude estimation. However, this test also shows that even after a loss of attitude knowledge the EKF can quickly redetermine the correct spacecraft attitude once OrCa2 returns to an orientation where the sun sensor face is within 60 degrees of perfect sun pointing.

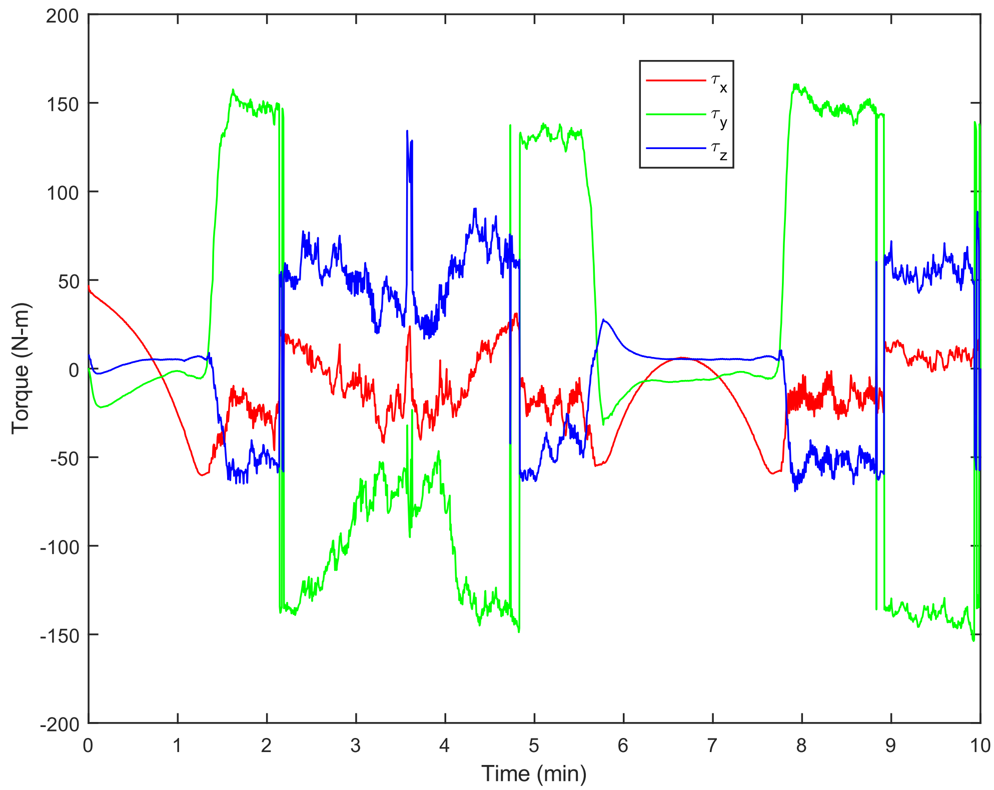

Figure 13. Commanded Controller Torques During Sun/Beacon Pointing Test.

As mentioned above, the imbalance of the test stand created a disturbance torque stronger than the magnetorquers could produce. However, Figure 13 shows that the commanded torques during the pointing test were in the correct direction to achieve sun pointing in the absence of large disturbances. At the start of the test when the engineering unit was rotated about the negative x-axis relative to the sun, the controller commanded a torque primarily about the positive x-axis. This commanded torque decreased as the engineering unit approached the sun pointing direction and changed directions when it rotated past the sun. The commanded torques were also in the correct direction to achieve sun pointing during the second pass when the sun was visible. The relationship between control torque and magnetic dipoles given by Eq. (17) applies to both the detumble and the sun/beacon pointing controller, so it is reasonable to assume that the same acceleration adjusted for disturbance torques computed from the detumble test can be achieved by either controller in the absence of large disturbances.

CONCLUSION

This report summarizes both the hardware and control algorithms utilized by the OrCa2 ADCS and describes the lab tests conducted to test these components. Coordination between sensors was successfully implemented to achieve accurate attitude estimation in the lab setting. The custom air coil magnetorquers built by the ADCS team were verified to produce torque sufficient to detumble the OrCa2 spacecraft from initial deployment spin within approximately two full orbits. A pointing control scheme was implemented to maintain constant sun pointing and nearly constant downlink antenna beacon pointing throughout the OrCa2 mission timeline to facilitate both maximum system battery charging and maximum beacon time. Flight data retrieved during the mission will be used by the team to verify the correct functioning of both the attitude estimation and control algorithms after launch.

ACKNOWLEDGEMENTS

I would like to thank Dr. Gunter for the opportunity to work on the OrCa2 mission and Harsh Patel for his countless hours of assistance with many of the tests described in this report and for doing a fantastic job as ADCS team lead.

REFERENCES

[1] Seiko Epson Corporation. "M-G364PDCA Data Sheet." May 2018.

[2] Honeywell. "1, 2 and 3 Axis Magnetic Sensors HMC1051/HMC1052/HMC1053." October 2018.

[3] Solar MEMS Technologies. "nanoSSOC-D60 Technical Specification, Interfaces & Operation." September 2015.

[4] Bellini, N., "Magnetic Actuators for Nanosatellite Attitude Control," thesis, Alma Mater Studiorum - Università di Bologna, 2014.

[5] Markley, F. L., and Crassidis, J. L., *Fundamentals of Spacecraft Attitude Determination and Control*. New York, New York: Springer, 2014.

[6] Alken, P., Thébault, E., Beggan, C.D. et al, "International Geomagnetic Reference Field: the thirteenth generation." *Earth, Planets and Space*. Springer, 2014. Vol. 73, No.49, 2021.